

JGR Space Physics

RESEARCH ARTICLE

10.1029/2021JA030003

Key Points:

- The occurrence of magnetospheric substorm clusters does not necessarily lead to radiation belt enhancements
- Substorm clusters during geomagnetically disturbed conditions ($AE > 100$ nT) reliably produce enhancements up to ultra-relativistic energies
- Whistler mode chorus intensities are larger during strongly disturbed substorm clusters than for moderate disturbances

Correspondence to:

C. J. Rodger,
crodger@physics.otago.ac.nz

Citation:

Rodger, C. J., Hendry, A. T., Clilverd, M. A., Forsyth, C., & Morley, S. K. (2022). Examination of radiation belt dynamics during substorm clusters: Activity drivers and dependencies of trapped flux enhancements. *Journal of Geophysical Research: Space Physics*, 127, e2021JA030003. <https://doi.org/10.1029/2021JA030003>

Received 28 SEP 2021

Accepted 6 DEC 2021

Examination of Radiation Belt Dynamics During Substorm Clusters: Activity Drivers and Dependencies of Trapped Flux Enhancements

Craig J. Rodger¹ , Aaron T. Hendry¹ , Mark A. Clilverd² , Colin Forsyth³ , and Steven K. Morley⁴ 

¹Department of Physics, University of Otago, Dunedin, New Zealand, ²British Antarctic Survey (UKRI-NERC), Cambridge, UK, ³UCL Mullard Space Science Laboratory, Dorking, UK, ⁴Space Science and Applications, Los Alamos National Laboratory, Los Alamos, NM, USA

Abstract Dynamical variations of radiation belt trapped electron fluxes are examined to better understand the variability of enhancements linked to substorm clusters. Analysis is undertaken using the Substorm Onsets and Phases from Indices of the Electrojet substorm cluster algorithm for event detection. Observations from low earth orbit are complemented by additional measurements from medium earth orbit to allow a major expansion in the energy range considered, from medium energy energetic electrons up to ultra-relativistic electrons. The number of substorms identified inside a cluster does not depend strongly on solar wind drivers or geomagnetic indices either before, during, or after the cluster start time. Clusters of substorms linked to moderate ($100 \text{ nT} < AE \leq 300 \text{ nT}$) or strong AE ($AE \geq 300 \text{ nT}$) disturbances are associated with radiation belt flux enhancements, including up to ultra-relativistic energies by the strongest substorms (as measured by strong southward B_z and high AE). These clusters reliably occur during times of high speed solar winds streams with associated increased magnetospheric convection. However, substorm clusters associated with quiet AE disturbances ($AE \leq 100 \text{ nT}$) lead to no significant chorus whistler mode intensity enhancements, or increases in energetic, relativistic, or ultra-relativistic electron flux in the outer radiation belts. In these cases the solar wind speed is low, and the geomagnetic Kp index indicates a lack of magnetospheric convection. Our study clearly indicates that clusters of substorms occurring outside of high speed wind streams are not by themselves sufficient to drive acceleration, which may be due to the lack of pre-cluster convection.

1. Introduction

It has long been recognized that electron fluxes in the outer radiation belt are highly dynamic. This high dynamism is thought to be due to competing drivers causing acceleration, loss, and transport, with growing evidence regarding the importance of nonlinear processes (see, e.g., the review, Ripoll et al., 2020). Typically, the occurrence and magnitude of the differing drivers are dependent upon distance from the Earth (expressed, e.g., through the L -shell), particularly due to the changing cold plasma density and the strong gradients around the plasmopause. At the same time, these driving processes also depend very strongly on magnetic local time (MLT). The drive to understand the spatial and temporal dynamism of the outer radiation belts encapsulates the primary science questions around that physical system.

A long-term focus for the radiation belt physics has been predicting the variation of trapped energetic and relativistic electron fluxes by understanding the physical processes driving the rapid, large magnitude changes seen in experimental data. About 15 years ago it was common for the community to try and understand changes occurring during very large geomagnetic disturbances, often looking at times around very large Dst changes. Unfortunately, this hampered deeper physical understanding of the processes occurring in the radiation belts, due to the combination of multiple large amplitude drivers competing during such large storms (Reeves et al., 2003). This focus on case studies during the largest disturbances has been described as the “Dst mistake” (Denton et al., 2009; Morley et al., 2010), summarized by Geoff Reeves with the expression “If you have seen one storm, you have seen one storm” (Koskinen, 2011, p. 323). Following the “Dst mistake,” there has been a stronger focus on trying to understand the “typical” or “consistent” variations in trapped fluxes when processes occur. One example of this approach is the use of superposed epoch analysis to focus electron flux decreases termed “dropouts,” seen in GPS data, following high speed streams (Morley et al., 2010), and subsequently examined using low-Earth POES observations (Meredith et al., 2011, Hendry et al., 2012). The value of similar approaches has been

demonstrated more recently in multiple studies, examples being: using Van Allen Probes to investigate the impact of differing drivers (Katsavrias, Daglis, & Li, 2019) and separating adiabatic and nonadiabatic effects (Murphy et al., 2018), MLT-resolved dynamics using POES measurements around substorm cluster events (Rodger et al., 2019), GPS-measured changes in electron fluxes during EMIC scattering events (Hendry et al., 2021), and BD-IES observed electron flux variations during high speed streams (Yin et al., 2019).

Changes in outer belt electron fluxes have been linked to clusters of substorms, termed "recurrent substorms" (Rodger et al., 2016), which show much more significant flux increases than is seen in single substorm events. Substorms are short-lived reconfigurations of the geomagnetic field where energetic particles are injected into the inner magnetosphere close to magnetic midnight (Akasofu, 1981; Cresswell-Moorcock et al., 2013). These injections include comparatively low energy source electrons that produce whistler mode chorus waves, a type of plasma wave recognized as a significant driver accelerating outer belt electrons to relativistic energies (e.g., Jaynes et al., 2015; Simms et al., 2018). Rodger et al. (2016), reported that in a statistical sense at the beginning of recurrent substorm clusters the IMF B_z turns southward, and that clusters occurred during times of high solar wind speeds. Rodger et al. (2016) also showed that, statistically, following the recurrent substorm clusters there are consistent and typical enhancements in lower band whistler mode chorus and energetic electron fluxes in the radiation belts. While both the chorus and flux enhancements started before the zero epoch, consistent with acceleration driven by enhanced magnetospheric convection driven by large-amplitude Alfvén waves in the solar wind (Lyons et al., 2005), there was a much stronger whistler mode chorus enhancement after the cluster onset, consistent with the importance of substorms providing source electrons. As noted previously, radiation belt processes are dynamic in L -shell as well as MLT; a follow-up study to Rodger et al. (2016), showed evidence for the MLT processes occurring in-situ (Rodger et al., 2019). These authors exploited the long lasting data sets of trapped energetic electron made by multiple Polar Orbiting Environmental Satellites (POES) low-Earth orbiting satellites producing 16,865 days worth of POES flux observations (i.e., >46 years of satellite observations). By focusing on medium energy electrons with energies of a few hundreds of keV (and therefore slow drift periods), it was possible to discriminate between processes occurring at different MLT, such as magnetopause shadowing, plasma wave activity, and substorm injections.

There is more frequent substorm activity during periods with fast, geoeffective solar wind (e.g., McPherron et al., 2009). Enhancements in radiation belt electron fluxes have been reported during times of prolonged substorm activity even in the absence of a geomagnetic storm (Meredith et al., 2003). Forsyth et al. (2016), showed that 50% of substorm intervals showed radiation belt enhancements within 24 h. It has also been shown that high speed solar wind conditions with southward IMF-dominant produces relativistic electron flux enhancements more effectively than northward IMF-dominant conditions (Miyoshi & Kataoka, 2008; McPherron et al., 2009). Many studies have identified the importance of whistler mode chorus waves in accelerating radiation belt electrons (e.g., Thorne, 2010; Ripoll et al., 2020), and these waves are known to be strongly correlated with magnetospheric substorms (e.g., Tsurutani & Smith, 1974; Meredith et al., 2003). Multiple studies have demonstrated that the intensity, occurrence, and MLT patterns for whistler mode chorus varies according to the AE index (e.g., Meredith et al., 2003; Li et al., 2009; Meredith et al., 2020).

Electron flux increases linked to clusters of substorms are not limited to the outer radiation belt. During even mildly geomagnetically disturbed periods, electrons ranging in energy from 10s of keV up to ~ 1 MeV can be quickly (in a few hours or less) injected into the slot and inner radiation belt ($L < 3$) in events termed SPELLS (sudden particle enhancements at low L shells) (Turner et al., 2017). Evidence has been shown that these injections may serve as the dominant source of 10s to 100s of keV electrons in Earth's inner radiation belt. Rodger et al. (2019), subsequently reported that SPELLS occur at times with high numbers of substorms, and also that the solar wind and geomagnetic changes around SPELLS times are very similar to those seen for recurrent substorm clusters. Rodger et al. (2019) suggested that SPELLS events are likely a subset of the recurrent substorm clusters, and are sufficiently common to appear in the typical (i.e., median) inner belt electron flux enhancements seen after these clusters (e.g., Rodger et al., 2016, Figure 4).

It is worth noting that the link between high speed streams, periods of high AE (expected during times of substorm clusters), and outer radiation belt relativistic electron enhancements was identified some time ago. The literature contains a series of papers investigating High-Intensity, Long-Duration, Continuous AE Activity (HILDCAA) events. This work initially identified HILDCAA activity present in the magnetosphere linked to large amplitude Alfvén waves in the solar wind and leading to intense auroral activity (Tsurutani & Gonzalez, 1987), with intense

substorm activity (Tsurutani et al., 1995, <https://doi.org/10.1029/95ja01476>). Subsequent work demonstrated that 94% of the HILDCAA periods were associated with high-speed solar wind streams (Hajra et al., 2013), much like the recurrent substorm clusters reported by Rodger et al. (2016, 2019), and that HILDCAA periods consistently produced enhancements in whistler mode chorus and relativistic electrons measured in geostationary orbit (Hajra et al., 2015).

In this paper we extend the works of Rodger et al. (2016, 2019) to better understand the variability of radiation belt enhancements linked to substorm clusters (as well as processes occurring before and after these clusters), and the link between these clusters and changing solar wind drivers. We advance the earlier approach of those authors by using an updated substorm cluster algorithm, improving the event detection quality, and expanding the time period of satellite data examined. We also check the validity of our findings by testing the observations from Low Earth Orbit (LEO) against measurements from Medium Earth Orbit (MEO) made much closer to the geomagnetic equator. The additional dataset allows a major expansion in the energy range considered, from the medium energy energetic electrons earlier reported on up to relativistic and ultra-relativistic electrons.

2. Experimental Datasets

2.1. POES SEM-2 Particle Observations

In this study the electron flux data is provided by the Polar Orbiting Environmental Satellites (POES). These are a constellation of LEO spacecraft (~800–850 km) in ~100-min period Sun-synchronous polar orbits. The POES spacecraft have monitored medium energy electron and proton fluxes using the Space Environment Monitor (SEM-2) package (Evans & Greer, 2004) since the launch of NOAA-15 in 1998. The specific observations we use come from the Medium Energy Proton and Electron Detector (Evans & Greer, 2004; Rodger, Clilverd, et al., 2010, Rodger, Carson, et al., 2010), which provide both trapped and precipitating electron observations. As shown by Rodger et al. (2010b) trapped flux measurements for radiation belt geomagnetic latitudes come from the 90-degree telescopes (named 90eX where X is the channel number (see Evans & Greer, 2004; Rodger, Clilverd, et al., 2010) for more details), while precipitating flux measurements for these latitudes come from the 0° telescopes (0eX).

During the period analyzed in our study (1 January 2005–30 Nov 2018) an increasing number of SEM-2 carrying POES spacecraft were launched, starting with the US NOAA-15 through to NOAA-19, and also the European MetOp-1 and 2 later in the time period. Unfortunately in the same period two POES were lost (NOAA-17 in 2013 and NOAA-16 in 2014). We choose the start of our time window to be 2005 so as to include at least three POES SEM-2 satellites to be operating (starting with NOAA 15–17), following Rodger et al. (2016). The choice of the end date was due to the timing of the start of this research work (in 2019), removing the last month of 2018 to ensure no epoch start times crossed into the following year. The raw POES dataset has 2 s resolution, with simultaneous measurements from multiple spacecraft. In this time period there are 25,947 file days worth of POES SEM-2 satellite data, equivalent to ~71 years of satellite observations.

Due to the large number of POES spacecraft, and their LEO orbits, there is very good coverage across L and MLT (e.g., Hendry et al., 2016, Figure 1). For the purposes of this study we have combined the MEPED observations from multiple POES satellites into an L and time grid of median flux values taking 0.25 L -resolution and 15 min time resolution. A more detailed description of the data set and the processing undertaken can be found in Rodger et al. (2010a) and Cresswell-Moorcock et al. (2013). As well as the zonal averaging into L and time bins mentioned earlier, this processing includes: the exclusion of observations made in the South Atlantic Magnetic Anomaly and during Solar Proton Events, and the correction of electron fluxes to compensate for proton contamination.

2.2. GPS Particle Observations

We also use electron flux data from the Combined X-ray Dosimeter (CXD) instruments carried by the majority of satellites in the Global Positioning System (GPS) constellation (Morley et al., 2017). At the time of writing, there are CXD data available for 25 of the GPS satellites, roughly covering the period 2001–2020. For our study we use the same time window as the POES satellites, from 2005 to 2018. The sampling rate of the CXD instrument is technically variable, however in practice the instrument has an accumulation time of 240s—this makes it ideal for

studying ultra-relativistic flux, which typically have fluxes too small to detect with shorter accumulation periods, however, it limits our ability to study short-duration phenomena.

The CXD instrument samples electron fluxes across 11 energy channels, from 120 keV to >6 MeV. The resultant electron counts are background corrected and converted to estimated differential fluxes using forward modeling; the accuracy of this modeling has been cross-calibrated against similar flux measurements from the Van Allen Probes (Morley et al., 2016). The result of this processing is a set of 15 differential, omnidirectional electron flux values spanning 15 energy levels from 120 keV to 10 MeV. For more information, see (Morley et al., 2016, 2017, Carver et al., 2020; Smirnov et al., 2020).

In our investigations of the GPS data, we use Roederer's generalized L-parameter L^* as opposed to McIlwain's L , calculated using SpacePy with a Tsyganenko-2005 magnetic field and the LANLstar neural network model (Hendry et al., 2021; Morley et al., 2011, 2019; Yu et al., 2012).

2.3. Demeter Lower-Band Chorus

We make use of observations from the ICE (Instrument Champ Electrique) instrument onboard the Demeter spacecraft to examine plasma wave activity. The Demeter satellite was launched in June 2004, flying at an altitude of 670 km (after 2005) in a Sun-synchronous orbit with an inclination of 98° , and deorbited in March 2011. We make use of data from June 2004 through to late December 2010. The ICE instrument produces continuous power spectrum measurements of one electric field component in the VLF band (Berthelier et al., 2006), in both survey and burst modes. The high-time resolution ICE/Demeter data has been re-processed to determine the hourly mean intensity of waves with $L = 0.25$ resolution in the frequency band from 0.1 to $0.5 f_{ce}$, where lower band chorus occurs. Note that Demeter has previously been used to study whistler-mode chorus, despite its comparatively low altitude (e.g., Santolík et al., 2006, Zhima et al., 2013; Rodger et al., 2016; Simms et al., 2021).

2.4. SOPHIE Clusters of Substorms

The SOPHIE algorithm examines the rate of decrease and increase of SuperMAG-L index (SML; Newell & Gjerloev, 2011a; Gjerloev, 2012) in order to identify substorm phases. In simple terms, substorm expansion phases are identified when the magnitude of the rate of decrease of SML exceeds some percentile threshold (EPT), although some data processing is applied to avoid short-term variations that are not expected to be related to substorm activity. In addition, the variation of the SuperMAG-U index (SMU) is compared to the SML index and events where this variation is similar are flagged as likely non-substorm events. Forsyth et al. (2015), provide substorm phase identifications for EPTs of 50%, 75%, and 90%, which correspond to decreases in SML of -3 , -8.5 , and -20 nT/min. From the average phase lengths given by Forsyth et al. (2015), this would result in substorm bays of 70, 180, and 350 nT respectively forming within ~ 30 min. As such, larger EPTs tend to identify more geomagnetically disturbed substorms. Using lower EPTs enhances the risk that small, substorm-like events (e.g., pseudo-breakups) are classified as substorms but gives greater confidence that all substorms are identified. In contrast, larger EPTs may miss some weaker substorm events but give greater confidence that the events identified are substorms and, in particular, that any clustering is a true clustering of substorm events rather than a sequence of small geomagnetic activity enhancements leading up to a full breakup, since each event needs to exceed the higher threshold in order to be identified.

We use the SOPHIE provided EPT = 90 expansion phase onset times to represent our substorm onset times, following the approach used earlier by Forsyth et al. (2015). This includes requiring that the rate of change of the SMU index is significantly different to that of the SML index during the expansion phase, as Forsyth et al. (2015) argued this was a useful test to avoid false identification. We also remove all events that occur during solar proton events, as the majority of radiation belt flux-measuring instruments provide highly unreliable observations during these times.

In order to identify “clusters” of substorms, we follow the same approach used earlier by Rodger et al. (2016, 2019), who followed the definition and naming convention of Newell and Gjerloev (2011b). This leads to a set of onset times of substorm clusters or chains termed “recurrent” substorm groupings. We use SOPHIE-derived recurrent substorm epoch start times spanning 1 January 2005 to 30 November 2018, thus including ~ 5 more years of coverage than the earlier SuperMAG based studies (that is, Rodger et al., 2016, 2019). However, the properties,

Table 1
Variation in the Number of Sophie-Reported Substorm Clusters, Through the EPT90 Expansion Phase Lists, and the Variation With AE Geomagnetic Index

	All AE	Quiet	Moderate	Strong
		AE \leq 100 nT	100 nT < AE \leq 300 nT	AE \geq 300 nT
Recurrent substorm epochs	2,749	591	1,283	881
Average # of onsets	2.4	2.2	2.3	2.5
Mean AE (nT)	261.4	60.8	188.4	502.6

Note. The criteria used to define the recurrent substorm epochs is given in Rodger et al. (2016). The mean number of SOPHIE-reported substorms in each recurrent substorm chain is given in the second line of the table (Average #), while the last line provides the mean AE value for the listed set of recurrent substorm epochs.

links to solar wind and geomagnetic activity, and radiation belt superposed epoch analysis are essentially identical to those described earlier in Rodger et al. (2016, 2019). We note that, unlike the identification of substorm onsets by Newell & Gjerloev (2011a), the SOPHIE algorithm identifies all substorm phases and does not explicitly specify a period within which no further onsets can be identified. This avoids potential misidentification of long, ongoing substorm expansion phases as recurrent substorms should the expansion phase extend beyond the time limit within which new onsets can be identified.

Table 1 provides a summary of the SOPHIE-derived recurrent substorm chains. Across the time period of interest there were a total of 16,763 SOPHIE determined substorm expansion phases meeting the EPT90 criteria. Following the selection outlined above, this leads to 2,749 recurrent substorm epoch start times, that is, 2,749 SOPHIE substorm clusters (2005–2018), an average of 197 per year, with a median cluster duration of 5 h. Note the SOPHIE cluster set equates to 34% more epochs than used in the earlier Rodger et al. (2016) study, who analyzed 2052 SuperMAG substorm clusters (2005–2013).

2.5. Solar Wind Observations and Geomagnetic Indices

In order to place the SOPHIE recurrent substorm events into a wider context, we make use of solar wind and geomagnetic disturbance observations. We undertake superposed epoch analysis (SEA) on the solar wind and geomagnetic drivers to investigate their variation around the SOPHIE recurrent substorm chains. The SEA process informs us of statistically “typical” behavior (i.e., median) around the zero epochs, hopefully providing insight into the physical processes coupling into the radiation belts. To do this, we take the zero epoch as the onset time of the first EPT90 substorm expansion phase in each chain. The result of the SEA is shown in Figure 1, investigating the variation in the solar wind speed, pressure, and density, the interplanetary magnetic field (IMF) B_z , and the geomagnetic indices SME, SMU, Kp, and Dst. Note that SME and SMU are the SuperMAG determined equivalents of the AE and AU indices, derived from approximately 110 ground-based magnetometers (Newell & Gjerloev, 2011a, 2011b). In all panels in this figure, the superposed epoch median of the plotted parameter is given by the solid black line and the 95% confidence interval for this median is shown by the red band. The dark blue bands mark the interquartile range and the 95% confidence interval about it (lighter blue).

Figure 1 of the current study should be contrasted with the right hand panels in Figure 1 of Rodger et al. (2016) and Figure 3 of Rodger et al. (2019). The panels in those figures showed the SEA for 2052 unique SuperMAG-determined recurrent substorm clusters which occurred from 2005 to 2013. Despite the differing source of the epoch lists (SuperMAG algorithm vs. SOPHIE), the differing time periods included (2005–2013 vs. 2005–2018), and the increased number of recurrent substorm clusters (2052 vs. 2749) the SEA results are essentially the same confirming the two approaches are examining highly similar conditions, as expected.

Figure 1 shows that the onset of the recurrent substorm clusters typically occur during periods of high solar wind speed, around the time of the peak in solar wind pressure and shortly before a minimum in solar wind density. The cluster-chain onset corresponds with a sharp southward turning in IMF B_z , as expected given that substorms are a loading-unloading response that occurs when the interplanetary magnetic field (IMF) turns southward. The SME index is sharply enhanced at this time, which is also expected as it is a SuperMAG-based improvement on the AE index, which itself is known to be a good indicator of the occurrence, strength, and duration of substorms (Gjerloev et al., 2004; Borovsky, 2016). Note that Kp is a good measure of convection (Thomsen, 2004), as is the AU index (e.g., Weimer, 1994), which is also enhanced at cluster onset. In contrast to these clear signatures, the median Dst at zero epoch only changes by a small amount, and even the quartile range does not reach levels associated with storm conditions (i.e., Dst \leq -50 nT).

In all the parameters plotted in Figure 1 there are clear signatures of typical behavior around these zero epoch times, with narrow confidence intervals around the median (shown in red). However, Figure 1 shows the quartile ranges are large, despite the consistent behavior of the medians. As an initial check, we investigated if the SEA

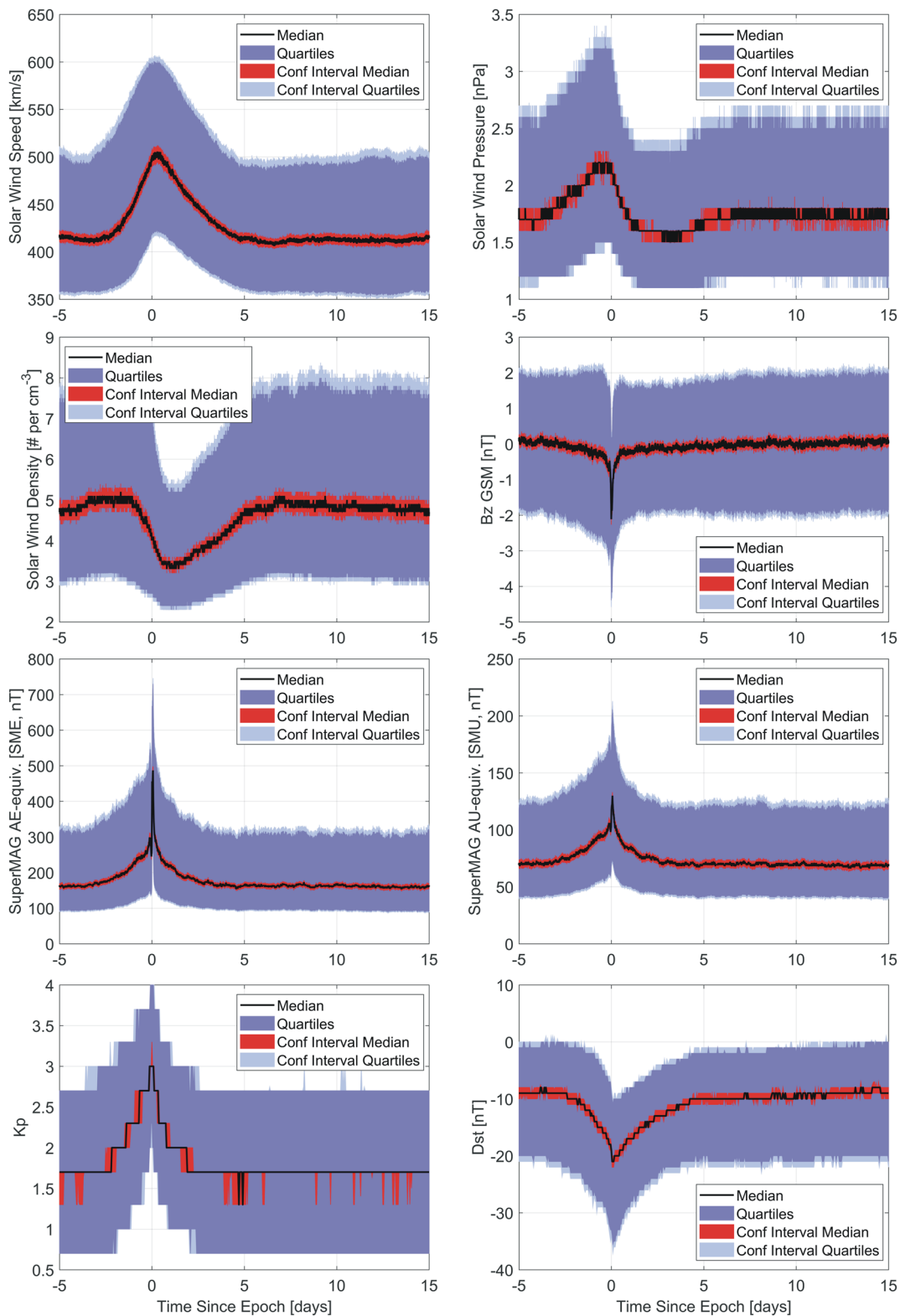


Figure 1. SEA showing the variation of the drivers for the SOPHIE Recurrent Substorm chains. The upper panels are the solar wind speed (left) pressure (right), respectively. The second set of panels show the solar wind density (left) and IMF B_z (right). The third set of panels is SuperMAG determined SME (left) and SMU (right). The lower set of panels show the varying Kp and Dst indices. In all cases the superposed epoch median of the plotted parameter is given by the solid black line. The 95% confidence interval for this median is shown by the red band. The dark blue bands mark the interquartile range and the 95% confidence interval about it (light blue).

median-responses vary strongly depending on the number of substorms in each cluster. Figure 2 shows the SEA of the same parameters presented in Figure 1, but now plotting the median value separately for each value of the number of unique substorm events inside a recurrent chain (from ≥ 2 to ≥ 6). Naively, we had expected that there would be significant changes visible in this plot, with larger substorm numbers corresponding to higher driving and larger events. In practice, we find this is not a useful way to examine the responses occurring around our epochs.

It is relatively common to examine various radiation belt processes (e.g., Douma et al., 2019; Zhao et al., 2019; Aryan et al., 2020) using the same three AE geomagnetic activity levels used in the chorus intensity studies (e.g., Meredith et al., 2003): quiet ($AE \leq 100$ nT), moderate ($100 \text{ nT} < AE \leq 300$ nT), and strong ($AE \geq 300$ nT). As such, we follow the same approach. Table 1 shows the number of recurrent substorm clusters whose AE-values at onset correspond to the quiet to strong AE ranges. About half of our recurrent substorm epochs correspond to moderate AE disturbances, slightly more than 20% are “quiet”, and the remainder strongly disturbed. Figure 3 shows the SEA of the solar wind and geomagnetic parameters used in Figures 1 and 2, now examining the responses during AE determined geomagnetic disturbances levels.

In contrast to Figure 2, SEA of the AE-dependent grouping of the SOPHIE substorm clusters leads to strong changes in the solar wind drivers and geomagnetic index responses, as seen in Figure 3. Despite the clusters being generated by the same algorithm, when the SEA of the solar wind drivers is considered based on the AE-value at the zero epoch there is a dramatic difference in all the parameters shown by the yellow lines in Figure 3. There is only a small increase in solar wind speed around the zero epoch for quiet AE substorm clusters, associated with very small solar wind pressure enhancements and density depletions. In this case, the IMF southward turning is comparatively weak, as is the SME enhancement. There is no clear enhancement in SMU or Kp for this group of substorm cluster epochs, suggesting very little magnetospheric convection is taking place, and there is no ring current response as seen in Dst.

The low solar wind drivers and geomagnetic indices seen for substorm clusters starting with quiet AE conditions are in strong contrast with the SEA for those parameters during moderate and strong AE conditions, seen by the red and blue lines in Figure 3, respectively. The solar wind speed and density variations are very similar when contrasting these two sets, although the peak solar wind pressure pulse is clearly lower for moderate conditions compared with strong. The same feature is seen in the magnitude of the IMF B_z value, which is clearly organized such that larger southward B_z values are typically for larger AE values. Similar organization is seen in SME and Kp, with increasing values, and hence convection, with increasing AE activity.

3. Radiation Belt Dynamics: Variation in Trapped Fluxes From LEO

3.1. AE-Dependent Variations

As noted above, it is fairly common to examine processes occurring in the radiation belts through the lens of geomagnetic disturbance ranges determined by AE. Given the strong difference in the AE-dependent SEA of solar wind drivers and geomagnetic indices seen in Figure 3, we make use of the same AE-ranges to organize SOPHIE substorm clusters and examine the variation in trapped fluxes reported by POES, that is, as seen from Low Earth Orbit. In this context the SEA process should clarify statistically “typical” behavior (i.e., median) of the radiation belts around our AE-dependent substorm clusters, hopefully providing insight into the physical processes dominating these changes. This is shown for the >300 keV electron flux observations from the 90e3 telescope in Figure 4. The left-hand side panels are the IGRF L -shell versus time plots, with the upper, middle, and lower rows corresponding to the quiet, moderate, and strong AE-ranges. The right-hand side panels presents the median, quartiles, and confidence intervals for the left-hand side plots, restricted to the outer radiation belts (L -shells ranging from 4.0-5.0), and for the corresponding AE-range. The colors used for the right-hand side panels are identical in meaning to those used in Figure 1. Note that the L -shell range is selected to better contrast across the varying AE-ranges, and also to compare with the GPS L^* observations shown in the later section.

In Figure 4, we focus on the >300 keV (i.e., 90e3) observations as it covers electron energies which are more traditional for radiation belt studies and allows better comparison with the GPS measurements reported in a later section. AE-dependent SEA undertaken for these epochs with the fluxes from >100 keV (i.e., 90e2) telescope produce results very similar to those seen in Figure 4, and hence are not shown.

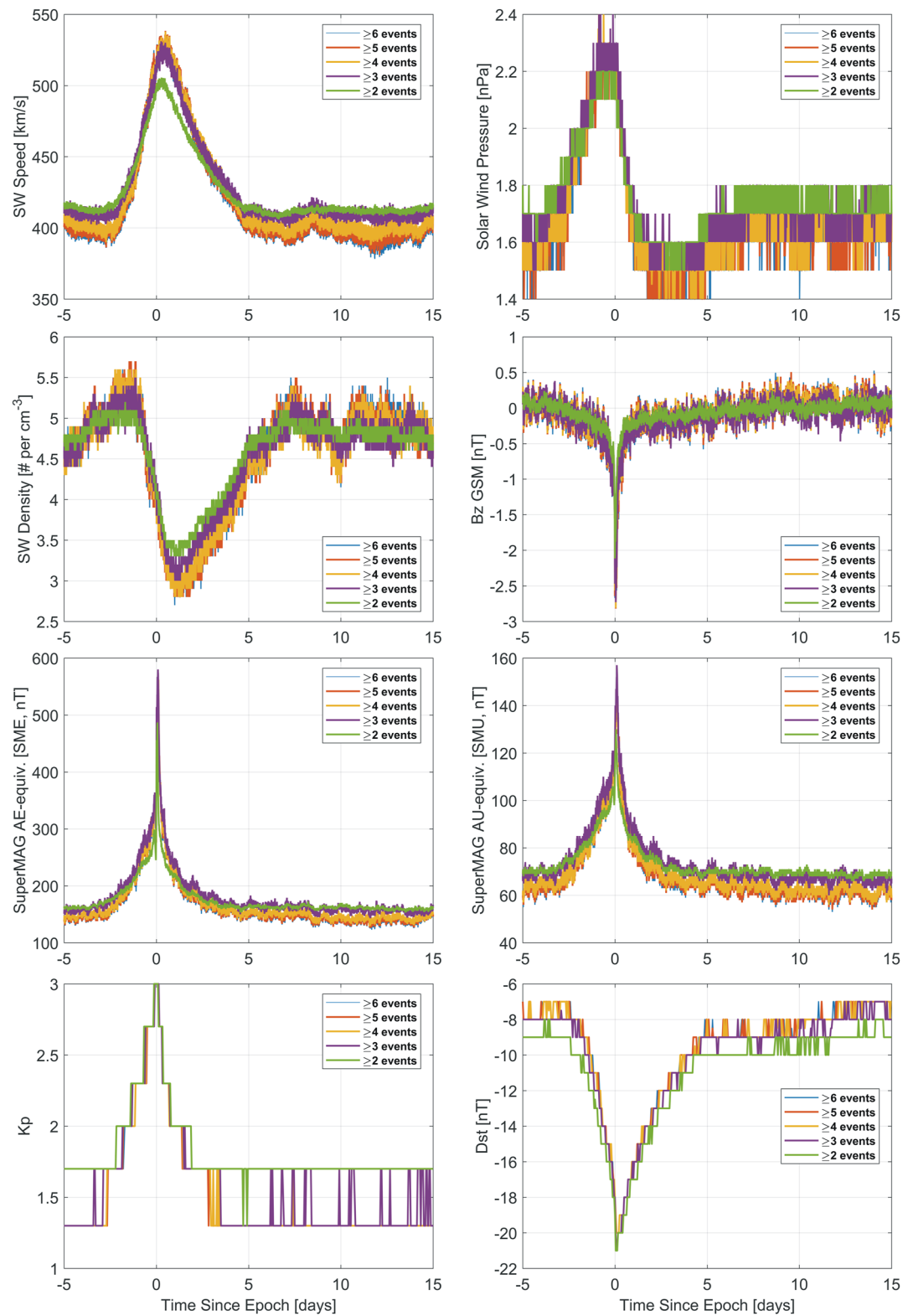


Figure 2. SEA showing the median variation of the drivers for the SOPHIE recurrent substorm chains, looking separately at the number of distinct substorms occurring in each recurrent cluster.

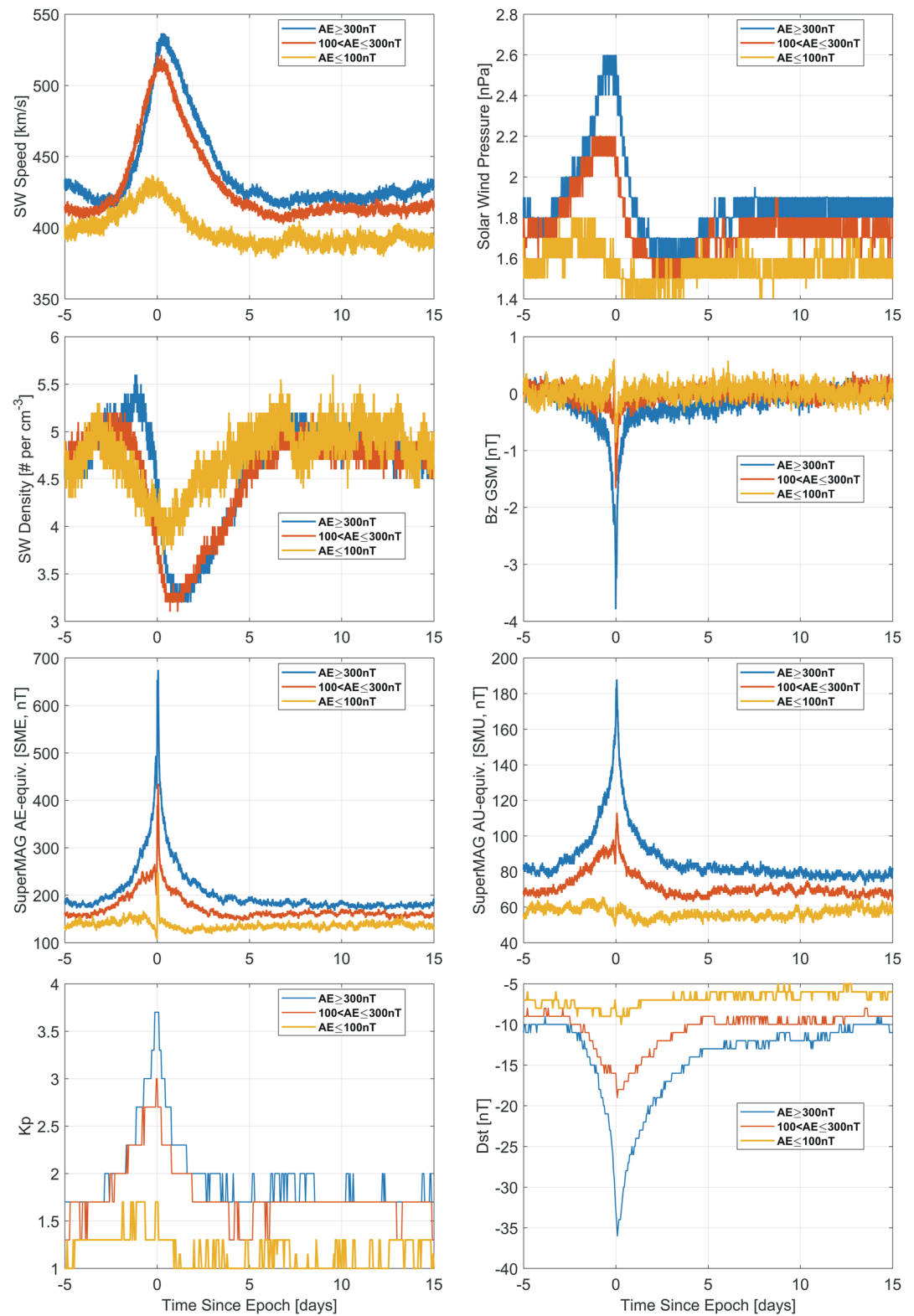


Figure 3. SEA showing the median variation of the drivers for the SOPHIE recurrent substorm chains, looking separately at three geomagnetic activity levels at the time of zero epoch as monitored by the AE index.

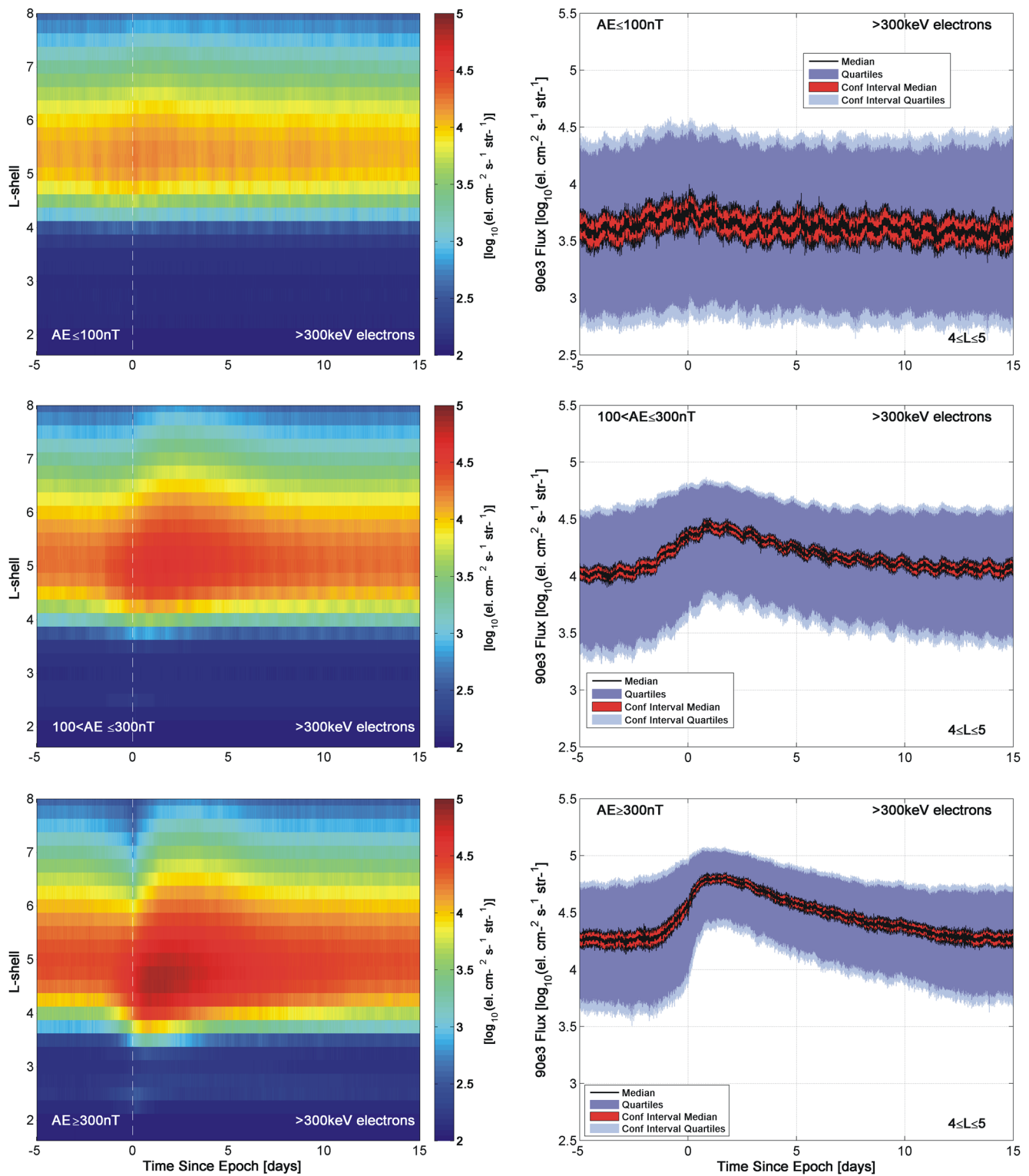


Figure 4. SEA showing the dynamics of the median >300 keV trapped electron flux variation from POES, looking separately at three geomagnetic activity levels at the time of zero epoch as monitored by the AE index. The left hand plots show the SEA of median trapped electrons for the AE dependent recurrent Substorm Epochs, plotted against L -shell. The right hand plots show the statistical variation of the outer radiation belt >300 keV fluxes in the L -shell range from 4.0 to 5.0. The median, quartiles, and confidence intervals are plotted in the same format as Figure 1.

Figure 4 shows strong difference in the trapped radiation belt electron fluxes around the times of recurrent substorm clusters, depending on AE-level. In the case of the quietest AE-range ($AE \leq 100$ nT, upper panels) there is almost no response in the >300 keV at and around the zero epoch, despite the occurrence of a cluster of substorms starting then. One can see a very small flux enhancement lasting 1–2 days in the upper left-hand panel of Figure 4, and a very slight increase in the L -shell range of the outer belt starting at the zero epoch. This change is too small to be visible in the accompanying right-hand panel, suggesting it is essentially insignificant.

The middle panel of Figure 4 presents the SEA for the moderate AE conditions ($100 \text{ nT} < AE \leq 300 \text{ nT}$). Starting from ~ 1 day before the zero epoch the >300 keV fluxes start to increase across the outer radiation belt, expanding across a wider L -shell range after the zero epoch. This flux enhancement lasts for ~ 12 – 13 days, and appears in these plots as a smooth increase followed by a smooth decrease.

The lower panel of Figure 4 presents the SEA for strong AE conditions ($AE \geq 300$ nT). The left-hand panel shows the electron flux enhancements start at approximately the same time as for moderate AE conditions (i.e., -1 day), but the enhancement is larger, and peaks lower in L -shell. There is also a sharp decrease in fluxes at high L starting shortly before the zero epoch, and lasting until ~ 1 day afterward, which extends to $L \sim 5.75$. The right panel has less structure than seen in the left hand panel, due to the L -shell range. The enhancement starts at ~ 1 day beforehand, as for moderate conditions, but there is a sharp discontinuity present at the time of the zero epoch in the form of a flux decrease. This is then followed by a rapid enhancement that is slightly larger when averaged from $L = 4.5$ – 6 than the moderate AE case and lasts until the ~ 13 days mark.

Note that the middle left-hand panel of this figure is very similar to the >300 keV panel of Figure 4 of Rodger et al. (2016) who undertook SEA for SuperMAG-reported substorm clusters without consideration of the differing AE responses. This is to be expected as the SOPHIE and SuperMAG substorm sets are expected to be equivalent on average, and the median responses for an all AE will be dominated by the moderate AE range (Table 1).

4. Radiation Belt Dynamics: Variation in Trapped Fluxes From MEO

The previous sections relied on the analysis of POES MEPED data collected from Low Earth Orbit. The POES LEO constellation has a number of advantages which make it suitable for the superposed epoch technique; the constellation is made up of a significant number of individual spacecraft, providing good MLT coverage and very long lasting measurement periods (i.e., large datasets). It is important to note, however, that the POES MEPED data suffer from disadvantages. Due to their LEO locations, the trapped fluxes measured by POES from the 90° telescopes are for electrons with pitch angles close to the edge of the drift loss cone, indeed for many subsatellite locations the 90° telescope will be sampling a mix of trapped and drift loss cone electrons (see the discussion in Rodger et al. (2010b, 2013)). In those locations is reasonable to expect the trapped electrons will strongly dominate the total flux measured, but due to the comparatively low equatorial pitch angles involved, the POES-reported trapped fluxes are likely to be a small fraction of the equatorial flux for the same field line. The POES MEPED data also suffer from limited energy resolution as the electron channels are integral and quite closely spaced, and rather low sensitivity (e.g., Yando et al., 2011).

For this reason, we wish to check our trapped flux conclusions using radiation belt observations from the GPS constellation, exploiting its higher altitudes (and hence larger population of trapped fluxes) and significantly enhanced energy resolution. The GPS measurements are plotted against the L^* parameter, rather than IGRF L . L^* is a magnetic drift invariant (Roederer, 1970); under adiabatic changes to the geomagnetic field L^* is a conserved quantity, and thus using L^* should minimize the influence of adiabatic changes. Due to the orbit of the GPS satellites, the L^* range of the CXD measurements is largely limited to $L^* > 4$.

The SEA of the GPS-observed trapped differential flux data is shown in Figure 5. The plot presents the three geomagnetic activity levels at the time of zero epoch as monitored by the AE index separately, as well as covering a range of electron energies spanning up to ultra-relativistic levels. In Figure 5, the AE-activity levels change from left to right panels (Quiet, Moderate, Strong), while the electron energy ranges change from top to bottom panels (300, 600, 1,000, 2,000, 5,000 keV). As noted above, the GPS SEA has been undertaken using L^* rather than IGRF L , as was used for POES. The results of this analysis are qualitatively similar when organized by L rather than L^* , as was previously reported earlier by Morley et al. (2010) for high speed solar wind stream driving

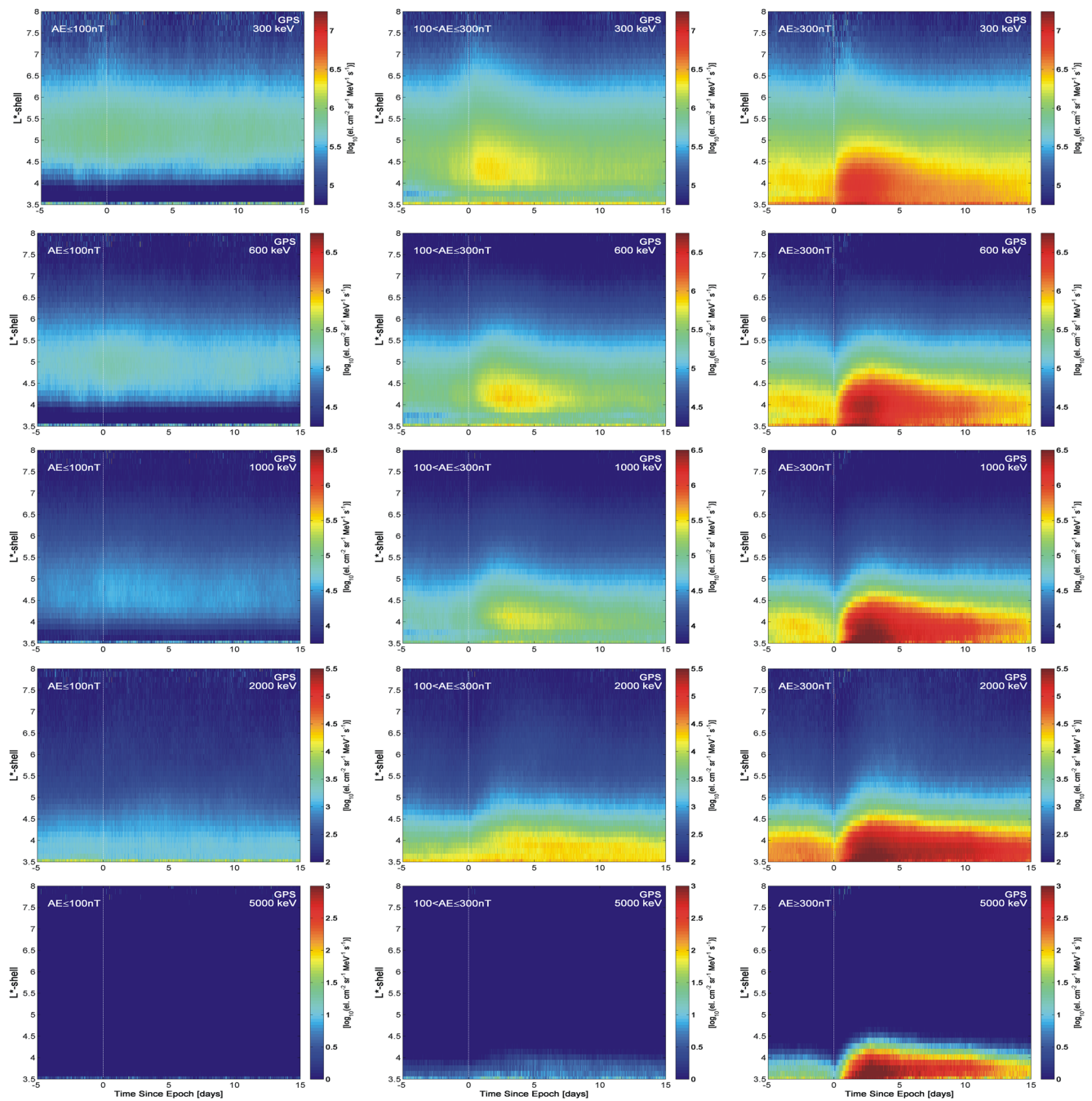


Figure 5. SEA showing the dynamics of the median trapped electron flux variation against L^* observed by GPS, looking separately at three geomagnetic activity levels at the time of zero epoch as monitored by the AE index. Energy ranges change from top to bottom (300, 600, 1,000, 2,000, 5,000 MeV), and the AE-activity level changes from left to right (Quiet, Moderate, Strong).

of the outer radiation belts. As sorting by L^* reduces the impact of any adiabatic changes, we take these data as being more physically meaningful.

The top set of panels in Figure 5 are for 300 keV electrons, which are most comparable to the left hand side panels of Figure 4. While the flux values, pitch angle range, and the units are different, the dynamical variations are very similar. Once again, the 300 keV GPS-observed flux variations are insignificant for quiet AE epochs, clearly enhanced following clusters of substorms with moderate AE levels, and significantly enhanced after substorm clusters associated with strong AE disturbances. In both GPS- and POES-observed medium energetic electrons

(i.e., 300 keV differential fluxes from GPS and >300 keV integral fluxes from POES) the enhancements move into the electron slot region, and there is also evidence of an electron dropout at high L -shells around the zero epoch times. These dropouts are consistent with the high speed stream dropouts in GPS fluxes reported by Morley et al. (2010). Similar dynamical changes are seen in the next set of GPS panels (600 keV), albeit with a slight delay relative to the zero epoch when compared with the 300 keV panel.

The top two lines of GPS flux panels in Figure 5 confirm the POES observations presented in Section 3, despite the very different altitude ranges and hence pitch angles sampled. In the three lower panels of Figure 5 we exploit the higher energy ranges sampled by GPS, investigating the relativistic and ultra-relativistic energy ranges. The fluxes for relativistic electrons (i.e., 1 MeV) is very similar to that seen for 300 and 600 keV. The ultra-relativistic flux panels (i.e., 2 and 5 MeV) show enhancements lasting progressively longer (>2 weeks), and peaking progressively later after the zero epoch, and occurring at lower L -shells. At even higher energies the relative flux enhancements (in terms of order of magnitudes) become more and more dramatic from quiet to strong AE, with near noise floor fluxes at 5 MeV for quiet epochs and all times, to an enhancement of greater than three orders of magnitude for strong AE epochs.

Figure 6 is the statistical variation of the outer radiation belt fluxes for $L^* = 4$ to 5 (i.e., the median, quartiles, and confidence intervals), in a format essentially the same as Figure 1. In this case however we have removed the black lines around the edges of the confidence intervals on the median; in Figure 6 the confidence intervals are so small that the inclusion of those black lines hides the red coloration for these confidence intervals. Once again, the upper row of panels in Figure 6 should be contrasted with the right hand panels of Figure 4; as expected from the strong agreement between Figure 5 and the left hand panels of Figure 4, the 300 keV GPS differential fluxes and >300 keV POES integral fluxes statistical changes are extremely similar, despite the altitude differences. The lower panels of Figure 6 again show that the stronger AE-epochs are linked to larger enhancements; the changing quartiles indicate that these responses are very typical for these events, with much larger flux enhancements for strong AE events post zero epoch and higher energies.

It is intriguing to note that in all cases the pre-zero epoch “background” fluxes are higher as the zero epoch AE values change from quiet to moderate to strong disturbances. This could be due to increasing pre-zero epoch convection, as evidenced by the SuperMAG AU and Kp values before the zero epoch time (as seen in Figure 3). It is reasonable to think that the differing pre-substorm cluster background fluxes will alter the acceleration occurring during the substorm, as multiple important radiation belt processes depend on initial conditions (termed “pre-conditioning”). We suggest this could be the focus of a future study and further detailed consideration.

5. Radiation Belt Dynamics: Variation in Lower Band Chorus

As noted earlier it has been suggested that the acceleration of the outer belt electrons may be caused by whistler mode chorus. The occurrence of chorus is dependent on electrons with energies of 1–10s of keV, which provide the “source” for whistler mode chorus activity. The availability of such electrons should be enhanced by magnetospheric convection, as well as substorm injections. Given the strong differences seen in the AE-dependent trapped flux response, it seems interesting to consider the variation in chorus activity. We examine this by considering the variation in lower-band chorus following the same approach we took in Section 3.1. Figure 7 shows the results of the superposed epoch analysis on Demeter measurements of lower-band chorus wave power, in a format similar to that of Figure 4 except showing wave power rather than particle flux. Note that as the Demeter satellite collected data for a shorter time period than POES satellite constellation has operated, we have had to restrict the SOPHIE epochs to the shorter time period.

The upper row of Figure 7 shows the superposed epoch analysis of the wave power in the lower band chorus frequency range for the quiet ($AE \leq 100$ nT) geomagnetic disturbance zero epochs. There is essentially no noticeable variation in chorus activity, consistent with the very low convection proxy activity (i.e., SuperMag AU and Kp) seen in Figure 3, and the lack of any significant trapped radiation belt electron increases seen in Figure 4. Despite the start of a cluster of substorms at the zero epoch, chorus power does not increase at this time. The very low levels of chorus frequency band power is consistent with earlier observations for similar AE-conditions (e.g., Meredith et al. (2012)), but is perhaps surprising given the zero epoch is the start of a cluster of substorms, and the suggestion that substorms are a “crucial element in the ultimate acceleration” process for relativistic electrons (Jaynes et al., 2015).

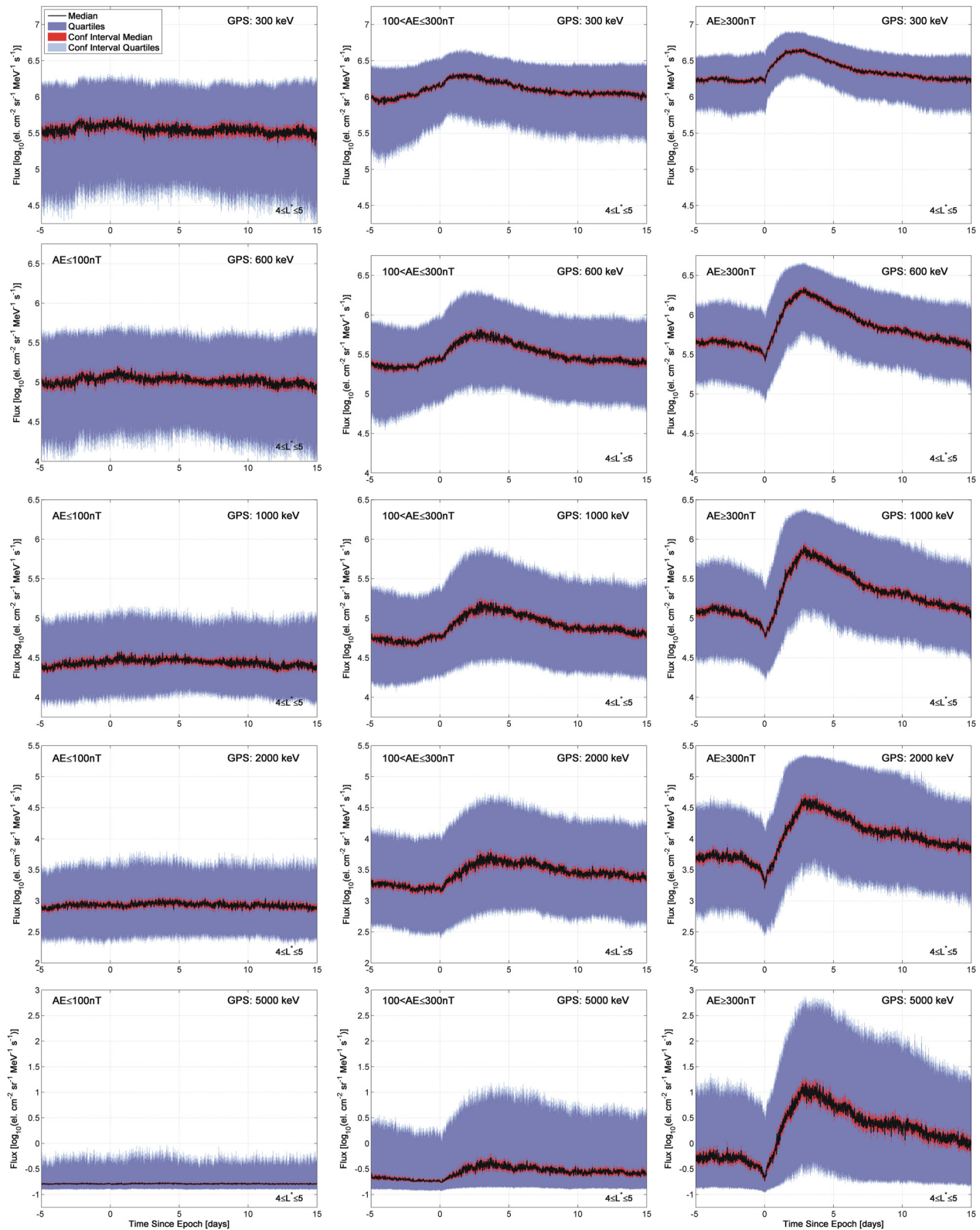


Figure 6. Statistical variation of the outer radiation belt fluxes observed by GPS spacecraft in the L^* -shell range from 4.0 to 5.0 undertaken on the fluxes shown in Figure 5. The median, quartiles, and confidence intervals are plotted in essentially the same format as Figure 1.

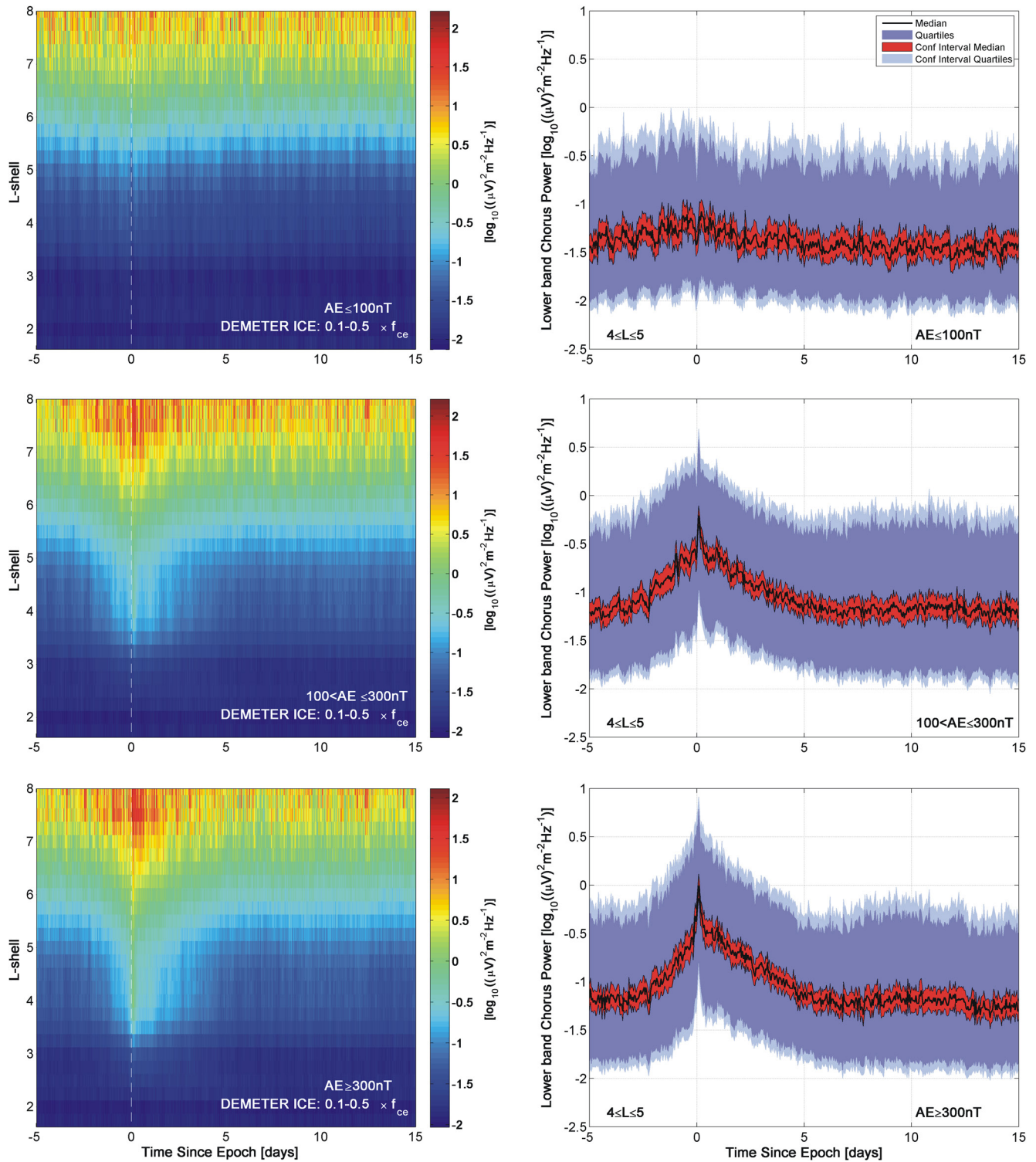


Figure 7. SEA showing the dynamics of the median Demeter lower-band chorus wave power observations, looking separately at three geomagnetic activity levels at the time of zero epoch as monitored by the AE index. This plot is in the same format as Figure 4, but presenting wave intensity data rather than particle flux.

The middle and lower panels of Figure 7 show the superposed epoch of Demeter-observed lower-band for moderate ($100 \text{ nT} < \text{AE} \leq 300 \text{ nT}$), and strong ($\text{AE} \geq 300 \text{ nT}$) geomagnetic disturbances. Both show an increase in power levels over $\sim 1\text{--}2$ days before the zero epoch, which is particularly similar to the time variation in the Kp convection proxy shown in Figure 3. This initial increase is of about 0.6 of an order of magnitude and is quite similar for both AE ranges. At the zero epoch there is a sudden and short-lived enhancement in chorus power seen in both the left hand and right panels. It is clear from the left hand panels that this chorus “spike” starting just after the zero epoch is larger for the stronger disturbances than for the moderate AE epochs. In the right panels we see an increase by another ~ 0.25 units for moderate AE epochs (on top of the slower increase before the zero epoch) and ~ 0.5 units for strong AE. After the short spike the chorus wave power returns to normal over ~ 5 days, with the power decay behaving in a very similar way for both moderate and strong AE conditions. For the lower two rows of Figure 7 the confidence intervals and quartiles suggest that this is very consistent and repeatable behavior, with the increase associated with the substorm-linked spike in chorus wave power being very similar in the median, with narrow confidence intervals around the median, and similar changes in the quartiles also.

We note that while the SuperMAG AU and Kp convection proxies are clearly lower for the moderate AE epochs when contrasted with the strong AE epochs, the Demeter observed chorus intensity levels are very similar up to the zero epoch, and also a few hours after the zero epoch. The primary difference between the moderate and strong AE epochs occurs in a narrow time period when the cluster of substorms occurs starting at the zero epoch.

6. Discussion

Figures 4 (POES) and 5 (GPS) indicate that clusters of substorms associated with moderate and strong geomagnetic disturbances (as measured by AE) are linked to trapped flux enhancements. These enhancements last $\sim 7\text{--}10$ days for subrelativistic electrons, increasing to >2 weeks for ultra-relativistic electrons. It is also notable that very similar responses are seen in both the LEO POES data and the near-equatorial GPS data, although this has been reported before, and attributed to the “global coherence of the radiation belts” (Kanekal et al., 2001).

While the flux increases are comparatively small for electron energies of a few hundred keV, which will dominate the POES-observed trapped fluxes shown in Figure 4, the GPS observations shown in Figures 5 and 6 indicate the outer belt electron flux enhancements are larger and better defined for higher energies, particularly for ultra-relativistic electron energies. In addition, the statistical variability of the outer radiation belt flux enhancement indicate that this is the common, repeatable flux behavior occurring after those substorm clusters. We argue this strongly suggests repeated and consistent physical processes up to and following the substorm cluster onsets leading to electron acceleration and relativistic and ultra-relativistic electron flux enhancements. This is clearly different from the oft-quoted challenge in radiation belt dynamics: “if you've seen one storm you've seen one storm” (e.g., Koskinen et al., 2017, but widely attributed to Geoff Reeves). But it is consistent with earlier findings that only $\sim 50\%$ of substorm intervals were followed by an enhancement in the radiation belts (as seen by changes in total radiation belt electron content) (Forsyth et al., 2016)

A possible mechanism to explain the post-substorm outer belt electron enhancements has been summarized by Jaynes et al., 2015 (Figure 1). They suggest that substorms provide an injection of “low-to medium-energy” electrons into the Earth's inner magnetosphere. The electrons of $1\text{--}10$ s of keV are termed “source” electrons with anisotropic angular distributions that provide energy for whistler mode chorus plasma waves. The chorus waves undergo wave-particle interactions with “seed” electrons, which are then accelerated to multi-MeV energies. The POES observations are consistent with these suggestions for $\text{AE} > 100 \text{ nT}$ substorm clusters (note that Rodger et al., 2016 previously showed that there is essentially no trapped flux response to isolated substorm events). There is an enhancement in >100 and >300 keV electron fluxes at the zero epoch, over a wide range of L -shells. The GPS data also suggests that the trapped 120 and 300 keV seed electron fluxes increase for ~ 2 days after the zero epoch, with higher energy electron fluxes rising more slowly and peaking later consistent with acceleration of the seed electron population. Jaynes et al. (2015) noted that the case study period they considered featured high, almost continuously fluctuating levels of AE activity, and thus were quite similar to the pattern of HILD-CAA events (Tsurutani et al., 1995), and were also consistent with analysis of Miyoshi and Kataoka (2008) who looked at the radiation belt flux responses for high speed solar wind periods separated by northward and southward-dominated IMF.

However, we feel it is important to note that our results are not entirely consistent with the Jaynes et al. (2015) mechanism outlined above. For the lowest AE range, there are no radiation belt enhancements, or indeed dynamic changes, seen by POES or GPS. As such the simple model suggesting substorms (or more accurately clusters of substorms) can trigger acceleration processes is too simple, but not entirely inaccurate. It appears the main difference between the quiet AE conditions and the moderate/strong conditions are found in the solar wind (Figure 3), particularly in the speed and pressure, and the magnitude of the southward IMF turning at the zero epoch. It appears that for those quiet conditions the substorm cluster, while present, does not inject significant source and seed electrons (>300 keV [Figure 4], and also for >100 keV [not shown]). That might cause the acceleration “pathway” to break down, due to the lack of seed electrons of a few hundred keV. Another possibility, however, comes from the lack of magnetospheric convection occurring before, during, and after the quiet AE substorm clusters, as seen through the AU and Kp indices in Figure 3. Without convection one would not have a pre-substorm enhancement of source electrons, and consequently the lack of observed whistler mode chorus at radiation belt L-shells (Figure 7). It is also intriguing to note that the chorus intensities pre-zero epoch are essentially the same for AE-moderate and -strong epochs, but the strong epochs have larger chorus intensities in the short period following the zero epoch substorms.

It may be that HILDCAA, recurrent substorm clusters, and SPELLS, are terms describing activity triggered by physically similar solar wind drivers impacting upon the inner magnetosphere. Those combination of drivers then appear to reliably cause significant radiation belt electron enhancements occurring in time periods that do not include major geomagnetic disturbances defined by Dst or Kp. However, we note that Tsurutani et al., 2004 found that while there were substorm expansions were present in the HILDCAA, there was no relationship to AE intensifications. This is an area which deserves further attention to better understand the context of the dynamical variations we have presented here.

We note that our observations may also been considered in the context of the “two-step acceleration” mechanism (see, e.g., Katsavrias, Sandberg, et al., 2019) where relativistic electrons (i.e., $\sim 1\text{--}2$ MeV) are a result of acceleration through wave-particle interactions with whistler mode chorus. Consequent enhancements in ultra-relativistic electrons (i.e., >3 MeV) are caused by the inward radial diffusion of those $1\text{--}2$ MeV electrons by ULF waves. The current study has not focused strongly on that acceleration idea, which is deserving of a more detailed consideration especially in terms of variation of Pc5 ULF waves. However, we note that in the current study we do not see a significant time delay between 2 and 5 MeV electron flux enhancements (Figures 5 and 6).

In the context of the wider literature, we note that the changing behavior of GPS-observed 300 keV electrons for $L^* = 4\text{--}5$ shown in the upper panels of Figure 6, is roughly consistent with the peak in the Van Allen Probes measured electron PSD of 100 MeV/G (which equates to ~ 300 keV electrons in the heart of the outer radiation belt) $\sim 24\text{--}48$ h after substorms (Nasi et al., 2020; Figure 8). However, in that Van Allen Probes-based statistical study, chorus amplitudes peaked $\sim 18\text{--}36$ h after the zero epoch (Nasi et al., 2020; Figure 4), and not a handful of hours later than the zero epoch as in our study. Some of this difference in the rapidly changing chorus SEA may arise from the differing choice of zero epoch in the two studies, as it appears the zero epoch in our study is roughly ~ 24 hr earlier than that used in Nasi et al. (2020).

7. Summary

In this study, we have examined dynamical variations in the radiation belt during times of mild geomagnetic disturbance during clusters of substorms. It is not uncommon for researchers to focus on strong storms to consider changes in the radiation belts; our results demonstrate that very mild disturbances are also associated with multiple processes leading to enhancements in flux over a wide range of energies stretching to ultra-relativistic levels. It is also not uncommon for researchers to suggest that substorms can trigger significant radiation belt flux enhancements by producing both the source and seed electron populations needed for acceleration to be geo-effective.

The current study indicates the difficulty in identifying simple mechanisms, like substorms or substorm clusters, which will consistently produce acceleration. When investigating substorm clusters, we find the number of substorms identified inside a recurrent cluster does not depend strongly on the solar wind drivers or geomagnetic indices before, during, or after the cluster start time.

We have found that there is a set of substorm storm clusters associated with quiet AE disturbances ($AE \leq 100$ nT) which lead to no significant chorus whistler mode intensity enhancements, or increases in energetic, relativistic, or ultra-relativistic electron flux in the outer radiation belts. Such substorm clusters are essentially “geo ineffective,” also lacking evidence of increased whistler mode chorus intensities. At these times solar wind speed is low, and the geomagnetic Kp and SMU indices are indicative of a lack of magnetospheric convection.

In contrast, clusters of substorms which occur linked to moderate ($100 \text{ nT} < AE \leq 300 \text{ nT}$) or strong AE ($AE \geq 300 \text{ nT}$) disturbances are clearly geoeffective in terms of radiation belt flux enhancements. These clusters reliably occur during times of high speed solar winds speeds with associated increased magnetospheric convection. Such clusters are associated with increased whistler mode chorus intensities both before and after the zero epoch; the principle difference in chorus intensity occurs shortly after the zero epoch, with strong epochs having higher chorus intensity than moderate epochs. This may suggest that the combination of increased magnetospheric convection and clusters of strong substorms (as measured by large B_z and high AE) are sufficient to provide radiation belt acceleration to ultra-relativistic energies. Statistical analysis of the radiation belt fluxes and whistler mode chorus intensities indicate these behaviors are typical for the geophysical conditions, with consistent variations seen in the medians, confidence intervals, and interquartile ranges.

The results above have been confirmed by examining radiation belt measurements made at LEO by POES, and contrasting it with near equatorial observations from the GPS constellation; both independent data sets confirm the relative geoeffectiveness of strong AE substorm clusters, with GPS confirming enhancements deep in the radiation belts of ultra-relativistic electrons.

Our study clearly indicates that clusters of substorms occurring outside of high speed wind streams are not by themselves sufficient to drive acceleration, which may be due to the lack of pre-cluster convection. Our study is unable to draw conclusions about time periods with strong convection with no-substorm activity as our zero epochs were selected based on SOPHIE-provided substorm lists.

Data Availability Statement

Data availability is described and accessible through the following websites: <https://www.ngdc.noaa.gov/stp/satellite/poes/dataaccess.html> (POES SEM observations), cdpp-archive.cnes.fr (DEMETER ICE), <https://www.ngdc.noaa.gov/stp/space-weather/satellite-data/satellite-systems/gps/> (GPS CXD V1.08), <http://supermag.jhuapl.edu/indices/> (solar wind parameters from SuperMAG), https://www.ukssdc.ac.uk/cgi-bin/wdcc1/secure/geophysical_parameters.pl (geomagnetic indices from the UK Solar System Date Centre).

Acknowledgments

The authors would like to thank the researchers and engineers of NOAA's Space Environment Center for the provision of the data and the operation of the SEM-2 instrument carried onboard these spacecraft over more than two decades. The authors also thank R. Gamble for preparing and J.-J. Berthelier for originally providing the DEMETER ICE data. The authors would like to thank the CXD team at Los Alamos National Lab-oratory who develop, maintain, operate, and process the GPS CXD data used in this study. The authors gratefully acknowledge the SuperMAG collaborators for providing the SML and SMU indices from which the SOPHIE events were derived. Colin Forsyth was funded by NERC IRF NE/N014480/1 and NERC grants NE/P017185/1 and NE/V002554/2. Contributions by Steven K. Morley were performed under the auspices of the US Department of Energy and partially supported by the Laboratory Directed Research and Development (LDRD) program, award 20190262ER.

References

- Akasofu, S. I. (1981). Energy coupling between the solar wind and the magnetosphere, *Space Science Reviews*, 28(2), 121–190. <https://doi.org/10.1007/BF00218810>
- Aryan, H., Agapitov, O. V., Artemyev, A., Mourenas, D., Balikhin, M. A., Boynton, R., & Bortnik, J. (2020). Outer radiation belt electron lifetime model based on combined Van Allen Probes and Cluster VLF measurements. *Journal of Geophysical Research: Space Physics*, 125, e2020JA028018. <https://doi.org/10.1029/2020JA028018>
- Berthelier, J. J., Godefroy, M., Leblanc, F., Malingre, M., Menvielle, M., Lagoutte, D., et al. (2006). ICE, the electric field experiment on DEMETER. *Planetary and Space Science*, 54(5), 456–471. <https://doi.org/10.1016/j.pss.2005.10.016>
- Borovsky, J. E. (2016). Solar wind-magnetosphere interaction, in *Space weather fundamentals*. Editor G. V. Khazanov (CRC Press), 47–73. <https://doi.org/10.1201/9781315368474-5>
- Carver, M., Morley, S. K., & Stricklan, A. (2020). GPS constellation energetic particle measurements, *2020 IEEE Aerospace Conference*, 1–10. <https://doi.org/10.1109/AERO47225.2020.9172652>
- Cresswell-Moorcock, K., Rodger, C. J., Kero, A., Collier, A. B., Clilverd, M. A., HÅggstrÅm, I., & PitkÅnen, T. (2013). A reexamination of latitudinal limits of substorm-produced energetic electron precipitation, *Journal Geophysical Research*, 118, 6694–6705. <https://doi.org/10.1002/jgra.50598>
- Denton, M. H., Borovsky, J. E., Horne, R. B., McPherron, R. L., Morley, S. K., & Tsurutani, B. T. (2009). Introduction to special issue on high speed solar wind streams and geospace interactions (HSS-GI). *Journal of Atmospheric and Solar-Terrestrial Physics*, 71, 1011–1013. <https://doi.org/10.1016/j.jastp.2008.09.019>
- Douma, E., Rodger, C. J., Blum, L. W., O'Brien, T. P., Clilverd, M. A., & Blake, J. B. (2019). Characteristics of relativistic microburst intensity from SAMPEX observations. *Journal of Geophysical Research: Space Physics*, 124, 5627, 5640. <https://doi.org/10.1029/2019JA026757>
- Evans, D. S., & Greer, M. S. (2004). *Polar orbiting environmental satellite space environment monitor - 2 instrument descriptions and archive data documentation*, NOAA technical Memorandum version 1.4, Space Environment Laboratory.
- Forsyth, C., Rae, I. J., Coxon, J. C., Freeman, M. P., Jackman, C. M., Gjerloev, J., & Fazakerley, A. N. (2015). A new technique for determining substorm onsets and phases from indices of the electrojet (SOPHIE), *Journal of Geophysical Research: Space Physics*, 120, 10592–10606. <https://doi.org/10.1002/2015JA021343>

- Forsyth, C., Rae, I. J., Murphy, K. R., Freeman, M. P., Huang, C.-L., Spence, H. E., et al. (2016). What effect do substorms have on the content of the radiation belts? *Journal of Geophysical Research: Space Physics*, *121*, 6292–6306. <https://doi.org/10.1002/2016JA022620>
- Gjerloev, J. W. (2012). The SuperMAG data processing technique. *Journal of Geophysical Research*, *117*, A09213. <https://doi.org/10.1029/2012JA017683>
- Gjerloev, J. W., Hoffman, R. A., Friel, M. M., Frank, L. A., & Sigwarth, J. B. (2004). Substorm behavior of the auroral electrojet indices. *Annales Geophysicae*, *22*, 2135–2149. <https://doi.org/10.5194/angeo-22-2135-2004>
- Hajra, R., Echer, E., Tsurutani, B. T., & Gonzalez, W. D. (2013). Solar cycle dependence of High-Intensity Long-Duration Continuous AE Activity (HILDCAA) events, relativistic electron predictors? *Journal of Geophysical Research: Space Physics*, *118*, 5626, 5638. <https://doi.org/10.1002/jgra.50530>
- Hajra, R., Tsurutani, B. T., Echer, E., Gonzalez, W. D., & Santolik, O. (2015). Relativistic ($E > 0.6$, >2.0 , and >4.0 MeV) electron acceleration at geosynchronous orbit during high-intensity, long-duration, continuous AE activity (HILDCAA) events. *The Astrophysical Journal*, *39*, 799. <https://doi.org/10.1088/0004-637X/799/1/39>
- Hendry, A. T., Rodger, C. J., Clilverd, M. A., Engebretson, M. J., Mann, I. R., Lessard, M. R., et al. (2016). Confirmation of EMIC wave-driven relativistic electron precipitation. *Journal of Geophysical Research: Space Physics*, *121*, 5366–5383. <https://doi.org/10.1002/2015JA022224>
- Hendry, A. T., Rodger, C. J., Clilverd, M. A., & Morley, S. K. (2021). Evidence of sub-MeV EMIC-driven trapped electron flux dropouts from GPS observations. *Geophysical Research Letters*, *48*, e2021GL092664. <https://doi.org/10.1029/2021GL092664>
- Hendry, A. T., Rodger, C. J., Clilverd, M. A., Thomson, N. R., Morley, S. K., & Raita, T. (2012). Rapid radiation belt losses occurring during high-speed solar wind stream-driven storms: Importance of energetic electron precipitation, 213, 224. In *Dynamics of the Earth's radiation belts and inner magnetosphere* (eds D. Summers, I. R. Mann, D. N. Baker, & M. Schulz). <https://doi.org/10.1029/2012GM001299>
- Jaynes, A. N., Baker, D. N., Singer, H. J., Rodriguez, J. V., Loto'aniu, T. M., Ali, A. F., et al. (2015). Source and seed populations for relativistic electrons: Their roles in radiation belt changes. *Journal of Geophysical Research: Space Physics*, *120*, 7240, 7254. <https://doi.org/10.1002/2015JA021234>
- Kanekal, S. G., Baker, D. N., & Blake, J. B. (2001). Multisatellite measurements of relativistic electrons: Global coherence. *Journal of Geophysical Research*, *106*(A12), 29721–29732. <https://doi.org/10.1029/2001JA000070>
- Katsavrias, C., Daglis, I. A., & Li, W. (2019). On the statistics of acceleration and loss of relativistic electrons in the outer radiation belt: A superposed epoch analysis. *Journal of Geophysical Research: Space Physics*, *124*, 2755–2768. <https://doi.org/10.1029/2019JA026569>
- Katsavrias, C., Sandberg, I., Li, W., Podladchikova, O., Daglis, I. A., Papadimitriou, C., et al. (2019). Highly relativistic electron flux enhancement during the weak geomagnetic storm of April–May 2017. *Journal of Geophysical Research: Space Physics*, *124*, 4402–4413. <https://doi.org/10.1029/2019JA026743>
- Koskinen, H. E. J. (2011). *Physics of Space storms: From the solar surface to the Earth*, Springer-Verlag, Springer Praxis Books Berlin, Heidelberg. https://doi.org/10.1007/978-3-642-00319-6_13
- Koskinen, H. E. J., Baker, D. N., Balogh, A., Gombosi, T., Veronig, A., & von Steiger, R. (2017). Achievements and challenges in the science of space weather. *Space Science Reviews* *212*, 1137–1157 (2017). <https://doi.org/10.1007/s11214-017-0390-4>
- Li, W., Thorne, R. M., Angelopoulos, V., Bortnik, J., Cully, C. M., Ni, B., et al. (2009). Global distribution of whistler-mode chorus waves observed on the THEMIS spacecraft. *Geophysical Research Letters*, *36*, L09104. <https://doi.org/10.1029/2009GL037595>
- Lyons, L. R., Lee, D.-Y., Thorne, R. M., Horne, R. B., & Smith, A. J. (2005). Solar wind-magnetosphere coupling leading to relativistic electron energization during high-speed streams. *Journal of Geophysical Research*, *110*, A11202. <https://doi.org/10.1029/2005JA011254>
- McPherron, R. L., Baker, D. N., & Crooker, N. U. (2009). Role of the Russell-McPherron effect in the acceleration of relativistic electrons. *Journal of Atmospheric and Solar-Terrestrial Physics*, *71*, 1032–1044. <https://doi.org/10.1016/j.jastp.2008.11.002>
- Meredith, N. P., Cain, M., Horne, R. B., Thorne, R. M., Summers, D., & Anderson, R. R. (2003). Evidence for chorus-driven electron acceleration to relativistic energies from a survey of geomagnetically disturbed periods. *Journal of Geophysical Research*, *108*, 1248. <https://doi.org/10.1029/2002JA009764>
- Meredith, N. P., Horne, R. B., Lam, M. M., Denton, M. H., Borovsky, J. E., & Green, J. C. (2011). Energetic electron precipitation during high-speed solar wind stream driven storms. *Journal of Geophysical Research*, *116*, A05223. <https://doi.org/10.1029/2010JA016293>
- Meredith, N. P., Horne, R. B., Shen, X.-C., Li, W., & Bortnik, J. (2020). Global model of whistler mode chorus in the near-equatorial region ($|\lambda| < 18^\circ$). *Geophysical Research Letters*, *47*, e2020GL087311. <https://doi.org/10.1029/2020GL087311>
- Meredith, N. P., Horne, R. B., Sicard-Piet, A., Boscher, D., Yearby, K. H., Li, W., & Thorne, R. M. (2012). Global model of lower band and upper band chorus from multiple satellite observations. *Journal of Geophysical Research*, *117*, A10225. <https://doi.org/10.1029/2012JA017978>
- Miyoshi, Y., & Kataoka, R. (2008). Flux enhancement of the outer radiation belt electrons after the arrival of stream interaction regions. *Journal of Geophysical Research*, *113*, A03S09. <https://doi.org/10.1029/2007JA012506>
- Morley, S. K., Sullivan, J. P., Henderson, M. G., Blake, J. B., & Baker, D. N. (2016). The Global Positioning System constellation as a space weather monitor: Comparison of electron measurements with Van Allen Probes data. *Space Weather*, *14*, 76–92. <https://doi.org/10.1002/2015SW001339>
- Morley, S. K., Friedel, R. H. W., Spanswick, E. L., Reeves, G. D., Steinberg, J. T., Koller, J., et al. (2010). Dropouts of the outer electron radiation belt in response to solar wind stream interfaces: Global positioning system observations. *Proceedings of the Royal Society A: Mathematical, Physical and Engineering Sciences*, *466*(2123), 3329, 3350. <https://doi.org/10.1098/rspa.2010.0078>
- Morley, S. K., Koller, J., Welling, D. T., Larsen, B. A., Henderson, M. G., & Niehof, J. T. (2011). Spacepy – a Python-based library of tools for the space sciences. In *Proceedings of the 9th Python in science conference (SciPy 2010)*.
- Morley, S. K., Niehof, J. T., Welling, D. T., Larsen, B. A., Haiducek, J., Killick, P., et al. (2019). *spacepy/spacepy: 0.2.1*. Zenodo. <https://doi.org/10.5281/zenodo.3252523>
- Morley, S. K., Sullivan, J. P., Carver, M. R., Kippen, R. M., Friedel, R. H. W., Reeves, G. D., & Henderson, M. G. (2017). Energetic particle data from the global positioning system constellation. *Space Weather*, *15*, 283–289. <https://doi.org/10.1002/2017SW001604>
- Murphy, K. R., Watt, C. E. J., Mann, I. R., Jonathan Rae, I., Sibeck, D. G., Boyd, A. J., et al. (2018). The global statistical response of the outer radiation belt during geomagnetic storms. *Geophysical Research Letters*, *45*, 3783–3792. <https://doi.org/10.1002/2017GL076674>
- Nasi, A., Daglis, I. A., Katsavrias, C., & Li, W. (2020). Interplay of source/seed electrons and wave-particle interactions in producing relativistic electron PSD enhancements in the outer Van Allen belt. *Journal of Atmospheric and Solar-Terrestrial Physics*, *210*, 105405. <https://doi.org/10.1016/j.jastp.2020.105405>
- Newell, P. T., & Gjerloev, J. W. (2011a). Evaluation of SuperMAG auroral electrojet indices as indicators of substorms and auroral power. *Journal of Geophysical Research*, *116*, A12211. <https://doi.org/10.1029/2011JA016779>
- Newell, P. T., & Gjerloev, J. W. (2011b). Substorm and magnetosphere characteristic scales inferred from the SuperMAG auroral electrojet indices. *Journal of Geophysical Research*, *116*, A12232. <https://doi.org/10.1029/2011JA016936>
- Reeves, G. D., McAdams, K. L., Friedel, R. H. W., & O'Brien, T. P. (2003). Acceleration and loss of relativistic electrons during geomagnetic storms. *Geophysical Research Letters*, *30*, 1529. <https://doi.org/10.1029/2002GL016513>

- Ripoll, J.-F., Claudepierre, S. G., Ukhorskiy, A. Y., Colpitts, C., Li, X., Fennell, J., & Crabtree, C. (2020). Particle dynamics in the Earth's radiation belts: Review of current research and open questions. *Journal of Geophysical Research: Space Physics*, *125*, e2019JA026735. <https://doi.org/10.1029/2019JA026735>
- Rodger, C. J., Carson, B. R., Cummer, S. A., Gamble, R. J., Clilverd, M. A., Green, J. C., et al. (2010). Contrasting the efficiency of radiation belt losses caused by ducted and nonducted whistler-mode waves from ground-based transmitters. *Journal of Geophysical Research*, *115*, A12208. <https://doi.org/10.1029/2010JA015880>
- Rodger, C. J., Clilverd, M. A., Green, J. C., & Lam, M. M. (2010). Use of POES SEM-2 observations to examine radiation belt dynamics and energetic electron precipitation into the atmosphere. *Journal of Geophysical Research*, *115*, A04202. <https://doi.org/10.1029/2008JA014023>
- Rodger, C. J., Cresswell-Moorcock, K., & Clilverd, M. A. (2016). Nature's Grand Experiment: Linkage between magnetospheric convection and the radiation belts. *Journal of Geophysical Research: Space Physics*, *121*, 171–189. <https://doi.org/10.1002/2015JA021537>
- Rodger, C. J., Kavanagh, A. J., Clilverd, M. A., & Marple, S. R. (2013). Comparison between POES energetic electron precipitation observations and riometer absorptions: Implications for determining true precipitation fluxes. *Journal of Geophysical Research: Space Physics*, *118*, 7810–7821. <https://doi.org/10.1002/2013JA019439>
- Rodger, C. J., Turner, D. L., Clilverd, M. A., & Hendry, A. T. (2019). Magnetic local time-resolved examination of radiation belt dynamics during high-speed solar wind speed-triggered substorm clusters. *Geophysical Research Letters*, *46*, 10219–10229. <https://doi.org/10.1029/2019GL083712>
- Roederer, J. G. (1970). *Dynamics of geomagnetically trapped radiation*. NY: Springer.
- Santolík, O., Chum, J., Parrot, M., Gurnett, D. A., Pickett, J. S., & Cornilleau-Wehrlin, N. (2006). Propagation of whistler mode chorus to low altitudes: Spacecraft observations of structured ELF hiss. *Journal of Geophysical Research*, *111*, A10208. <https://doi.org/10.1029/2005JA011462>
- Simms, L., Engebretson, M., Clilverd, M., Rodger, C., Lessard, M., Gjerloev, J., & Reeves, G. (2018). A distributed lag autoregressive model of geostationary relativistic electron fluxes: Comparing the influences of waves, seed and source electrons, and solar wind inputs. *Journal of Geophysical Research: Space Physics*, *123*, 3646–3671. <https://doi.org/10.1029/2017JA025002>
- Simms, L. E., Engebretson, M. J., Rodger, C. J., Dimitrakoudis, S., Mann, R., & Chi, P. J. (2021). The combined influence of lower band chorus and ULF waves on radiation belt electron fluxes at individual L-shells. *Journal of Geophysical Research: Space Physics*, *126*, e2020JA028755. <https://doi.org/10.1029/2020JA028755>
- Smirnov, A. G., Berrendorf, M., Shprits, Y. Y., Kronberg, E. A., Allison, H. J., Aseev, N. A., et al. (2020). Medium energy electron flux in Earth's outer radiation belt (MERLIN): A machine learning model. *Space Weather*, *18*(11), e2020SW002532. <https://doi.org/10.1029/2020SW002532>
- Thomsen, M. F. (2004). Why Kp is such a good measure of magnetospheric convection. *Space Weather*, *2*, S11004. <https://doi.org/10.1029/2004SW000089>
- Thorne, R. M. (2010). Radiation belt dynamics: The importance of wave-particle interactions. *Geophysical Research Letters*, *37*, L22107. <https://doi.org/10.1029/2010GL044990>
- Tsurutani, B. T., & Gonzalez, W. D. (1987). The cause of high-intensity long-duration continuous AE activity (HILDCAAs): Interplanetary Alfvén wave trains. *Planetary Space Science*, *35*, 405–412. [https://doi.org/10.1016/0032-0633\(87\)90097-3](https://doi.org/10.1016/0032-0633(87)90097-3)
- Tsurutani, B. T., Gonzalez, W. D., Gonzalez, A. L. C., Tang, F., Arballo, J. K., & Okada, M. (1995). Interplanetary origin of geomagnetic activity in the declining phase of the solar cycle. *Journal of Geophysical Research*, *100*, 21717–21733. <https://doi.org/10.1029/95JA01476>
- Tsurutani, B. T., Gonzalez, W. D., Guarnieri, F., Kamide, Y., Zhou, X., & Arballo, J. K. (2004). Are high-intensity long-duration continuous AE activity (HILDCAA) events substorm expansion events? *Journal of Atmospheric and Solar-Terrestrial Physics*, *66*, 167–176. <https://doi.org/10.1016/j.jastp.2003.08.015>
- Tsurutani, B. T., & Smith, E. J. (1974). Postmidnight chorus: A substorm phenomenon. *Journal of Geophysical Research*, *79*(1), 118–127. <https://doi.org/10.1029/JA079i001p00118>
- Turner, D. L., O'Brien, T. P., Fennell, J. F., Claudepierre, S. G., Blake, J. B., & Jaynes, A. N. (2017). Investigating the source of near-relativistic and relativistic electrons in Earth's inner radiation belt. *Journal of Geophysical Research: Space Physics*, *122*, 695–710. <https://doi.org/10.1002/2016JA023600>
- Weimer, D. R. (1994). Substorm time constants. *Journal of Geophysical Research*, *99*(A6), 11005–11015. <https://doi.org/10.1029/93JA02721>
- Yando, K., Millan, R. M., Green, J. C., & Evans, D. S. (2011). A Monte Carlo simulation of the NOAA POES medium energy proton and electron detector instrument. *Journal of Geophysical Research*, *116*, A10231. <https://doi.org/10.1029/2011JA016671>
- Yin, Z., Zou, H., Ye, Y., Zong, Q., & Wang, Y. (2019). Superposed epoch analysis of the energetic electron flux variations during CIRs measured by BD-IES. *Space Weather*, *17*, 1765–1782. <https://doi.org/10.1029/2019SW002296>
- Yu, Y., Koller, J., Zaharia, S., & Jordanova, V. (2012). L^{*} neural networks from different magnetic field models and their applicability. *Space Weather*, *10*(2). <https://doi.org/10.1029/2011sw000743>
- Zhao, W., Liu, S., Zhang, S., Zhou, Q., Yang, C., He, Y., et al. (2019). Global occurrences of auroral kilometric radiation related to suprathermal electrons in radiation belts. *Geophysical Research Letters*, *46*, 7230–7236. <https://doi.org/10.1029/2019GL083944>
- Zhima, Z., Cao, J., Liu, W., Fu, H., Yang, J., Zhang, X., & Shen, X. (2013). Demeter observations of high-latitude chorus waves penetrating the plasmasphere during a geomagnetic storm. *Geophysical Research Letters*, *40*, 5827–5832. <https://doi.org/10.1002/2013GL058089>